THE JOURNAL OF PHYSICAL CHEMISTRY C

Article

Cite This: J. Phys. Chem. C 2018, 122, 115−123

pubs.acs.org/JPCC

Distinguishing Thermal and Electronic Effects in Ultrafast Optical Spectroscopy Using Oxide Heterostructures

Sergey Y. Smolin,[†] Amber K. Choquette,[‡] Jiayi Wang,[‡] Steven J. May,[‡] and Jason B. Baxter*[,†]

[†]Department of Chemical and Biological Engineering and [‡]Department of Materials Science and Engineering, Drexel University, Philadelphia, Pennsylvania 19104, United States

Supporting Information

ABSTRACT: Measuring time-resolved photoexcited properties in semiconductors is critical to the design and improvement of light-harvesting devices. Although ultrafast pump−probe spectroscopy offers a promising route to understand carrier recombination mechanisms and quantify lifetimes, thermal contributions to the transient optical response can be significant and need to be properly accounted for to isolate carrier-induced contributions. We demonstrate the use of broadband ultrafast optical spectroscopy on type I heterostructures as a means to isolate transient effects that are solely thermal in nature. Specifically, we use transient absorption and reflectance spectroscopy to measure the time-resolved optoelectronic changes in photoexcited epitaxial bilayers of $LaFeO_3$/$LaMnO_3$ and monolithic thin films of these materials. Experiments and complementary numerical modeling reveal that thermal effects dominate the transient absorption and reflectance spectra above the band gap. Fitting the dynamics with a thermal diffusion model yields thermal conductivities of 6.4 W m^{-1} K^{-1} for $LaFeO_3$ and 2.2 W m^{-1} K^{-1} for $LaMnO_3$. In $LaFeO_3$, an additional photoinduced absorption feature below the band gap at ∼1.9 eV is assigned primarily to photoexcited carriers and persists for over 3 ns. This work provides a direct demonstration of how thermal and electronic contributions can be separated in transient optical spectroscopies, enabling new insights into dynamical optical properties of semiconductors.

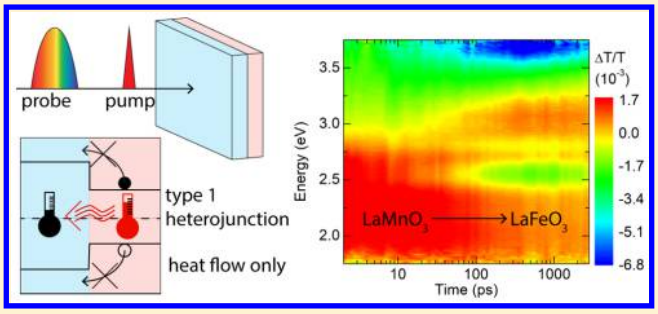

I. INTRODUCTION

Ultrafast transient absorption and reflectance (TA/TR) spectroscopies are foundational techniques for studying photoexcited carrier lifetimes, interfacial transfer rates, and recombination mechanisms.[1] Because quantifying photoexcited carrier dynamics is central to the design and improvement of light harvesting devices, these transient optical techniques have been applied to a wide range of semiconductors.[1−14] However, interpretation of transient absorption and reflectance data is not always straightforward because the optical response can arise from multiple electronic and thermal effects.

In a typical TA/TR experiment, the sample is photoexcited with an ultrafast pump pulse and the differential transmission or reflection is measured with reference to the nonphotoexcited sample. Some features of the differential spectra have electronic origins, such as ground state bleaching due to bandfilling, stimulated emission, and photoinduced absorption.[15] However, heat released as photoexcited carriers thermalize can also have a large influence on optical properties and hence the differential spectra, even at very low fluences.[6,7,16] These thermally induced transients in the optical spectrum compete with carrier-induced effects,[17] as shown schematically in Figure 1. During thermalization, electron−phonon scattering transfers heat to the lattice within ∼1 ps following excitation.[6,18,19] This heat typically expands the lattice, broadens electronic bands,[20] and red-shifts the absorption edge, creating complicated optical transients.[16] In contrast, ground state bleaching due to bandfilling typically blue-shifts the absorption edge near the band gap.[17] Additionally, photoexcited carriers can have new absorption pathways at photon energies that are smaller than the band gap due to free carrier absorption. Heating also confounds the interpretation of the dynamics of the optical response. Diffusion of heat across thin films occurs on the same picosecond to nanosecond time scales that are often characteristic of carrier recombination. Furthermore, carriers and heating are coupled through nonradiative recombination.

Previous research has highlighted the inherent difficulty in decoupling thermal and electronic phenomena and demonstrated several strategies to address this challenge. Sabbah et al. investigated silicon single crystals using degenerate transient optical spectroscopy to pump and probe at 1.55 eV, above the indirect band gap.[7] They modeled time-resolved transient reflectance data with coupled thermal and carrier diffusion equations, taking advantage of the fact that surface recombination was the only recombination mechanism on the 100 ps time scales measured. They found that heat injected into the lattice following surface recombination had a significant contribution to the transient optical response, especially at

Received: September 27, 2017
Revised: December 6, 2017
Published: December 7, 2017

DOI: 10.1021/acs.jpcc.7b09592
J. Phys. Chem. C 2018, 122, 115−123

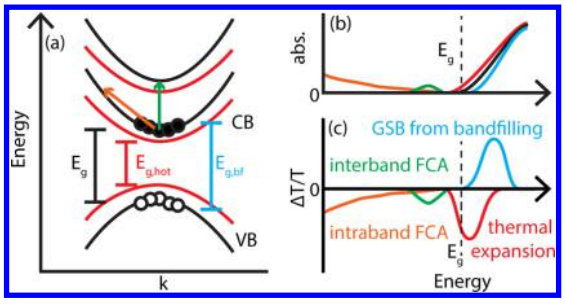

Figure 1. Schematic comparing thermal and several electronic contributions to the (a) band structure, (b) absorption profile, and (c) resulting differential transmission spectrum. The position of the band gap, E_g, is marked with a dashed line in (b) and (c). Thermal expansion (red curves) typically leads to red-shifting of the band gap, labeled $E_{g,hot}$, and broadening of the electronic band structure which manifest as decreased light transmission close to the band gap. Band filling (blue curves) with photoexcited carriers has a contrasting effect, effectively blue-shifting the band gap, $E_{g,bf}$, and leading to a ground state bleach (GSB) (increased light transmission) just above the band gap. Intraband free carrier absorption (orange curves) traditionally follows a Drude $1/E^2$ dependence, while interband free carrier absorption (green curves) can be observed below the band gap through new absorption pathways. The actual spectral positions and shapes are highly dependent on the band structure of the semiconductor. Schematics not drawn to scale.

high surface recombination velocities. More recently, Sheu et al. investigated thermal effects in single crystals of multiferroic $BiFeO_3$ by varying the amount of excess energy of pump photons.[6] Probing above the 2.7 eV band gap at 3.12−3.23 eV, they found that the temperature rise in the film had a strong influence on the optical response within picoseconds and persisted for longer than 1 ns.[6]

Decoupling thermal and carrier effects can be even more challenging in materials where thermal diffusion and carrier recombination occur on similar picosecond to nanosecond time scales, as is the case for many thin films. However, a broadband probe can facilitate decoupling by identifying spectral signatures that arise mainly from heating or from carriers. For example, Hayes et al. used a combination of broadband transient absorption spectroscopy and temperature-dependent ellipsometry to clarify the physical origins of TA dynamics in hematite (Fe_2O_3) thin films.[16] Previous literature over two decades had predominantly assigned spectral features to photoexcited carriers, regardless of hematite morphology or environment.[14,21−24] However, Hayes et al. demonstrated that for thin films in air TA signals beyond the first picosecond in the visible range were mainly due to heating. The critical piece of evidence was their comparison of transient absorption spectra to *ex situ* thermal difference spectra obtain from spectroscopic ellipsometry. Only a small spectral shoulder below the 2.4 eV band gap at 1.8 eV was assigned to photoexcited carriers, which persisted for less than 100 ps. While reports of carrier lifetimes of nanoseconds or more are reasonable for *in situ* measurements of hematite photoanodes under bias,[24] such long dynamics in thin films should be attributed to lattice cooling, rather than carrier recombination as previously assigned.[21,25] Such work highlights the use of broadband probes and the importance of decoupling thermal and electronic contributions to the transient spectra to accurately describe ultrafast processes.

In this work, we demonstrate the use of semiconductor heterostructures to distinguish thermal and carrier effects by taking advantage of band alignments that enable heat flow—but not electron or hole transfer—between materials. As shown schematically in the inset of Figure 2, by exciting the smaller band gap material in the type I heterostructure, only heat can flow to the larger band gap material, allowing thermal diffusion to be monitored in the larger band gap material using transient optical spectroscopy. Thermal effects can be isolated by comparing transient optical spectra and kinetics derived solely from heat to those derived from a combination of heat and photoexcited carriers that arise upon direct photoexcitation. The advantage of using electronically engineered bilayers is that the same experimental technique (broadband TA or TR spectroscopy) can be used to monitor both the diffusion of heat and the recombination of photoexcited carriers. Furthermore, because the thermal difference spectra are time-resolved, thermal conductivities can be quantified by modeling heat transfer.

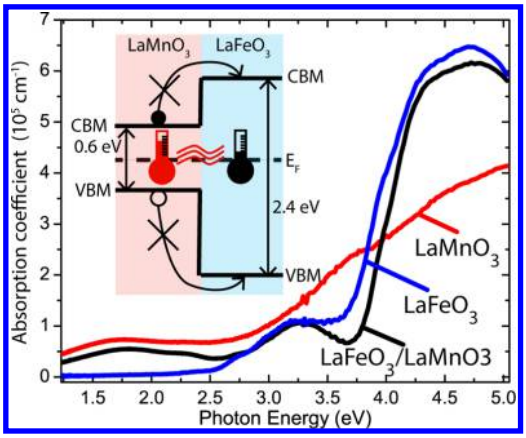

Figure 2. Optical absorption for $LaMnO_3$ (21.9 nm), $LaFeO_3$ (16.5 nm), and a $(LaFeO_3)_{52}/(LaMnO_3)_{51}$ (20.9 nm/20.2 nm) heterostructure, each grown on LSAT. Inset shows the type I band alignment of $LaFeO_3$ and $LaMnO_3$ with a valence band offset of 1.2 eV and a conduction band offset of 0.6 eV, as determined previously.[29] A type I heterojunction allows heat flow but not carrier transfer to the larger band gap material following photoexcitation of the smaller band gap material.

We illustrate our approach combining transient optical spectroscopy and temperature-dependent ellipsometry on single-layer and thin film heterostructures of $LaFeO_3$ and $LaMnO_3$—two perovskite oxide semiconductors that have well-studied electronic structure and diverse physical properties[26−28] and that have a type I band alignment.[29] Traditionally, inorganic perovskite oxides with the chemical formula ABO_3 have been studied for their magnetic, ionic, and electronic properties,[30−32] but they are increasingly investigated for their light-harvesting potential.[33−38] Indeed, this chemically flexible class of oxides has band gaps that are tunable from ultraviolet to near-infrared[39−41] as well as other unique properties such as ferroelectricity that make them promising candidates for photovoltaic and photocatalytic applications.[33,42] $LaFeO_3$ and $LaMnO_3$ are stable, nontoxic, and strong absorbers of light, with band gaps of ∼2.4 eV[43] and ∼0.6 eV.[29] $LaFeO_3$ has already been utilized for photocatalytic applications.[15,38,44,45] We have previously reported on ultrafast dynamics of $LaFeO_3$ thin films[46] but did not adequately account for thermal effects, and this work provides a chance to revisit that material. We are unaware of any previous study of subnanosecond-scale transient

DOI: 10.1021/acs.jpcc.7b09592
J. Phys. Chem. C 2018, 122, 115−123

optoelectronic properties in $LaMnO_3$. Here we find that thermal contributions dominate the transient absorption and reflectance spectra in the visible light range from 2.2 to 3.8 eV for both materials, and a thermal diffusion model reveals thermal conductivities of 6.4 W m^{-1} K^{-1} for $LaFeO_3$ and 2.2 W m^{-1} K^{-1} for $LaMnO_3$. Additionally, carriers in $LaFeO_3$ produce a photoinduced absorption feature below the band gap at ∼1.9 eV that persists for nanoseconds.

II. EXPERIMENTAL METHODS AND MODELING

Epitaxial thin films of $LaFeO_3$, $LaMnO_3$, and $(LaFeO_3)_n/(LaMnO_3)_m$ bilayers were grown on double-side polished $La_{0.3}Sr_{0.7}Al_{0.65}Ta_{0.35}O_3$ (LSAT) (001) substrates via molecular beam epitaxy,[29] where the subscripts n and m indicate the number of unit cells of each layer. The c-axis lattice parameter for the films is 4.00 ± 0.02 Å per unit cell; further details were reported previously.[29] Scanning transmission electron microscopy and X-ray scattering showed the high crystalline quality and sharp (<2 nm) interfaces,[29] making these heterostructured films well-suited for ultrafast spectroscopic investigation. The samples measured in this work are the same as those in ref 29, where a more detailed discussion of their growth and characterization is given. Static optoelectronic properties in the visible range, 1.2−5 eV, were measured by variable angle spectroscopic ellipsometry (J.A. Woolam M-2000U). The measured Ψ and Δ were fit using WVASE32 software to extract the index of refraction (n) and extinction coefficient (k) of the films at several temperatures from 25 to 300 °C. The absorption coefficient, α, was calculated by $\alpha = 4\pi k/\lambda$, where λ is the incident photon wavelength.

Broadband ultrafast transient absorption and reflectance spectroscopy were used to measure dynamic optoelectronic properties. The output of a regeneratively amplified Ti:sapphire laser (Coherent Libra, 50 fs, 1 kHz, 3.5 W) was split to generate a tunable pump pulse using an optical parametric amplifier (Coherent OPerA Solo) and a broadband probe pulse using white light continuum generation in sapphire and CaF_2 crystals in the transient absorption spectrometer (Ultrafast Systems Helios). The pump photoexcites carriers in the material, and the probe pulse interrogates the sample's optoelectronic properties after a time delay controlled by an optical delay line. Every other pump pulse is blocked with a chopper, allowing photoexcited properties to be isolated from ground state properties. The experimental method relies on monitoring the time-resolved differential reflectance or transmission. In transient absorption spectroscopy, the change in transmitted light is calculated as $\frac{\Delta T}{T} = \ln\left(\frac{I_{ex,T}}{I_{0,T}}\right)$, where T is transmission, I is the intensity of light, and subscripts ex and 0 represent the excited and nonexcited state. It is also common to see transient absorption data reported as $\Delta A = -\ln(10)\frac{\Delta T}{T}$. When the intensity of reflected probe light is monitored, the differential reflectance is calculated as $\frac{\Delta R}{R} = \ln\left(\frac{I_{ex,R}}{I_{0,R}}\right)$, where R represents reflectance.

III. RESULTS AND DISCUSSION

Probing Heating Effects with Monolithic and Heterostructured Thin Films. Static optical absorption spectra provide insight into the band structure of the semiconductors and guidance on interpretation of ultrafast spectral transients. The optical absorption spectra for $LaFeO_3$, $LaMnO_3$, and a $(LaFeO_3)_{52}/(LaMnO_3)_{51}$ bilayer film are shown in Figure 2. Consistent with previous work, $LaFeO_3$ exhibits a band gap of ∼2.4 eV and a higher energy transition at ∼3.5 eV.[43] $LaMnO_3$ exhibits a band gap of ∼0.6 eV[29] and a higher energy absorption edge at ∼3.0 eV. Using hard X-ray photoelectron spectroscopy,[29] we previously found a type I band alignment with a valence band offset of 1.2 eV and a conduction band offset of 0.6 eV.

The broadband transient absorption data for $LaFeO_3$, $LaMnO_3$, and the $(LaFeO_3)_{52}/(LaMnO_3)_{51}$ bilayer films grown on LSAT are shown in Figure 3. The $LaFeO_3$ data exhibit three distinct regions of decreased light transmission at 1.9, 2.5, and 3.5 eV. The latter two correspond to the band gap and higher energy transition in $LaFeO_3$. Likewise, $LaMnO_3$ has two distinct spectral transients: decreased light transmission at ∼3 eV that matches the higher energy transition in the absorption data and a region of increased light transmission at ∼2 eV. Analogous spectral features can be seen in the transient reflectance spectra shown in the Supporting Information, Figure S1.

Figure 3e,f shows the TA data for a $(LaFeO_3)_{52}/(LaMnO_3)_{51}$ bilayer photoexcited with 1.55 eV photons. This photon energy is sufficient to excite carriers only in $LaMnO_3$. Therefore, immediately following excitation, the TA spectra strongly resemble the spectra from monolithic $LaMnO_3$ excited at 1.55 eV as shown in Figure 3c,d. However, the spectral weight in the bilayer film shifts over the next 3 ns to strongly resemble the TA spectra of $LaFeO_3$ excited at 4 eV, as shown in Figure 3a,b. Although 1.55 eV photons can excite carriers from the $LaMnO_3$ valence band to the $LaFeO_3$ conduction band, this excitation pathway would be confined to the interface and is expected to be minimal compared to the bulk excitation in $LaMnO_3$.

Photoexciting the $LaMnO_3$ layer within the bilayer at 1.55 eV and 1.0 mJ/cm^2 initially increases the average temperature of $LaMnO_3$ by 11 K, assuming that all the excitation energy above the band gap is converted into heat as carriers relax to the band minimum (see Supporting Information). Because $LaFeO_3/LaMnO_3$ forms a type I heterostructure, the majority of photoexcited carriers are confined to $LaMnO_3$ following their rapid thermalization (∼1 ps). Therefore, the $LaFeO_3$-like features in the bilayer spectral response are thermal in origin, arising as the heat released from carrier cooling in $LaMnO_3$ diffuses into $LaFeO_3$. The thermally derived spectral peaks for $LaFeO_3$ are marked with dashed lines at ∼2.5 and ∼3.6 eV in Figure 3a,c and can also be seen in the 1 ns spectral slices. Monolithic $LaMnO_3$ does not display these features at ∼2.5 or ∼3.6 eV.

To confirm the effect of heating on optical properties in $LaFeO_3$, we measured the *ex situ* thermal difference spectra with temperature-dependent, variable-angle spectroscopic ellipsometry from the monolithic $LaFeO_3$ film. The thermally derived $\frac{\Delta T}{T}$ and $\frac{\Delta R}{R}$ spectra were calculated from the measured n and k using eqs S1 and S2 in the Supporting Information. The $\frac{\Delta T}{T}$ spectrum for $LaFeO_3$ for a temperature difference of 175 °C is shown in Figure 4a (red line) and for several other temperature differences up to 275 °C in Figure S2. The thermal difference spectrum has two areas of decreased light transmission at ∼2.5 and ∼3.6 eV, with increased transmission at ∼3.0 eV. The thermal difference spectrum from ellipsometry is similar to the TA spectra generated by photoexcitation in Figures 3a,b and 4a (black line), supporting the dominant effect of heating on the TA spectra above the band gap. The excess

DOI: 10.1021/acs.jpcc.7b09592
J. Phys. Chem. C 2018, 122, 115−123

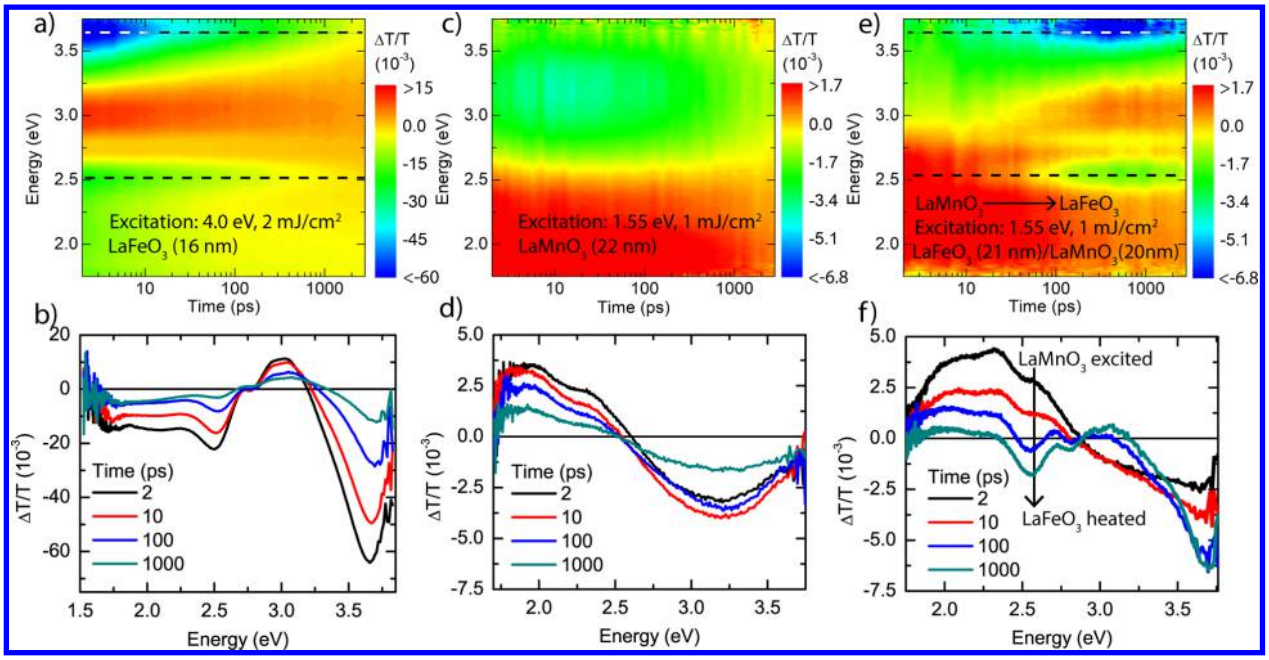

Figure 3. TA data for (a) $LaFeO_3$/LSAT pumped at 4.0 eV and 2 mJ/cm^2; (c) $LaMnO_3$/LSAT pumped at 1.55 eV and 1 mJ/cm^2; and (e) $(LaFeO_3)_{52}/(LaMnO_3)_{51}$/LSAT pumped at 1.55 eV and 1 mJ/cm^2. (b), (d), and (f) show spectral slices of these TA data at several times ranging from 2 to 1000 ps for $LaFeO_3$, $LaMnO_3$, and the $(LaFeO_3)_{52}/(LaMnO_3)_{51}$ bilayer, respectively.

photon energy relative to the band gap for the pump conditions of Figure 3a,b initially increases the temperature of the $LaFeO_3$ film by roughly 60 K (see Supporting Information). Based on the ellipsometry data in Figure S2, a 60 K increase in $LaFeO_3$ temperature results in a $\frac{\Delta T}{T}$ signal of −0.06 at ∼3.6 eV, which is consistent with the magnitude of the TA transient 2 ps after excitation. Moreover, the ellipsometry data in Figure S2 show a blue-shift in spectral peaks as the temperature decreases. A similar shift in the TA spectra occurs with increasing delay time as the heat diffuses from the film into the substrate, corroborating that thermal effects dominate the TA response for $LaFeO_3$ above the band gap. Thermal effects also dominate the transient reflectance above the band gap, as shown in Figures S2b and S3, in contrast to our previous incorrect interpretation that electronic effects play the predominant role in dynamic optical phenomena in $LaFeO_3$ photoexcited above its band gap.[43]

While thermal effects dominate the optical response above the band gap, a subgap photoinduced absorption can be assigned to photoexcited carriers in $LaFeO_3$. Figure 4a compares a TA spectrum of photoexcited $LaFeO_3$ (black), which could include contributions from both heat and carriers, to two spectra that can only be derived from heating—a thermal difference spectrum of $LaFeO_3$ from ellipsometry (red) and a TA spectrum of the $LaFeO_3/LaMnO_3$ bilayer after excitation of $LaMnO_3$ (blue). The bilayer spectrum (blue) represents the thermally induced spectrum derived from TA and was calculated by subtracting the measured $LaMnO_3$ TA spectrum (Figure 3d) from the measured $LaFeO_3/LaMnO_3$ TA spectra (Figure 3f), with both spectra taken 1 ns after excitation. All spectra in Figure 4a were normalized by the peak at ∼3.6 eV to facilitate comparison. Raw data are shown in Figure S4. Below the band gap of 2.4 eV, the TA spectra of the monolithic $LaFeO_3$ film cannot be reproduced by thermal effects alone. This difference implies that electronic effects contribute within this spectral region and that dynamics will depend on trapping and recombination of photoexcited carriers.

The sign and energy of the broad feature at ∼1.9 eV in $LaFeO_3$ are consistent with intraband free carrier absorption. To validate this assignment, we varied the photon energy of the pump to manipulate the amount of excess energy per carrier. As photoexcited carriers cool to the conduction band minimum, they release heat equivalent to the excess excitation energy above the band gap of the semiconductor. Figure 4b shows TA spectra of monolithic $LaFeO_3$ excited with photon energies of 4.0, 3.1, and 2.7 eV, resulting in 1.6, 0.7, and 0.3 eV of excess energy per electron. These spectra were recorded 2 ps after excitation to allow enough time for carriers to transfer energy to the lattice, but not enough time for heat to diffuse significantly into the substrate. Because we hypothesize that the below-band gap feature originates from photoexcited carriers, the spectra were normalized to the peak of this region (near 1.9 eV) to facilitate comparison on a per-carrier basis. As less excess energy is injected into the lattice, less spectral weight is dedicated to the thermal feature at ∼2.5 eV relative to the photoinduced absorption feature at ∼1.9 eV.

By subtracting the normalized thermally derived TA spectrum for $LaFeO_3$ in the $LaFeO_3/LaMnO_3$ bilayer (Figure 4a, blue line) from the normalized TA spectrum for monolithic $LaFeO_3$ (Figure 4a, black line), we can approximate the nonthermal component of the TA spectrum. This nonthermal spectrum is shown in green in Figure 4b, labeled $\Delta\left(\frac{\Delta T}{T}\right)$, and has a similar spectral shape to the $LaFeO_3$ excited with minimal excess energy at 2.7 eV. This further corroborates that the photoinduced absorption below the band gap of $LaFeO_3$ is due to photoexcited carriers. This assignment is similar to recent hematite literature, where the spectral region below the band gap in Fe_2O_3 was also assigned to photoexcited carriers, while the above-gap response in that material was found to have a thermal origin.[16] The substrate may also add spectral weight to the region below the band gap, and we quantify the

DOI: 10.1021/acs.jpcc.7b09592
J. Phys. Chem. C 2018, 122, 115−123

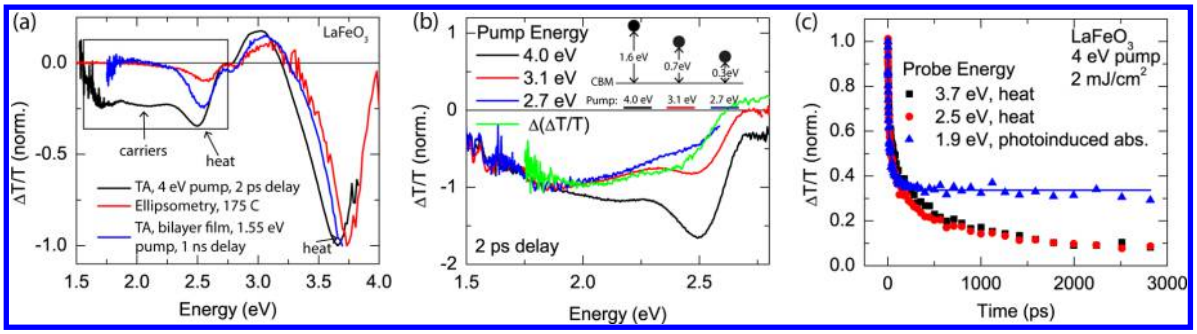

Figure 4. (a) Normalized transient absorption spectra derived from photoexcited carriers and heat for $LaFeO_3$. Black curve was pumped at 2 mJ/cm^2, and the blue curve was pumped at 1 mJ/cm^2. (b) TA spectra of $LaFeO_3$ excited with different photon energies to modulate the heat per carrier following excitation. At energies closer to the band gap, the relative spectral weight associated with heating at ~2.5 eV decreases compared to the electronic feature at ~1.9 eV. The green curve, labeled $\Delta\left(\frac{\Delta T}{T}\right)$, was calculated by subtracting the blue curve from the black curve in (a) and approximates the carrier-induced spectral signature in $LaFeO_3$. In (b), pump fluences for 4, 3.1, and 2.7 eV were 2.4, 0.9, and 0.8 mJ/cm^2. (c) Normalized kinetics probed in $LaFeO_3$ at 3.7 eV (heating), 2.5 eV (heating), and 1.9 eV (carriers). The thermal regions have nearly identical dynamics, whereas decay of the photoinduced absorption below the band gap is considerably slower. Traces were normalized to the signal at 2 ps following excitation.

contribution as up to one-fourth of the observed magnitude at 1 ns, as explained further in the Supporting Information and shown in Figure S5. State filling of any electronic structure within the band gap would lead to decreased absorption, or increased light transmission, across that energetic transition, which is not consistent with the sign of our data below the band gap. Thus, the sign of the transient below the band gap is indicative of free carrier absorption, which could arise as photogenerated electrons are excited higher in the conduction band (or holes excited lower in the valence band).

Monitoring the decay of the TA spectral features enables insight into both carrier dynamics and heat transfer in $LaFeO_3$. Figure 4c shows that the decay of the thermally derived features at ~2.5 and ~3.6 eV are nearly identical, as expected because both features originate from heating. The signal decays by 80% within the first 500 ps and continues to decay further with time. In contrast, the feature at 1.9 eV assigned to carriers shows slower dynamics, again suggesting that this feature does not originate from heating in $LaFeO_3$. The signal probed at 1.9 eV decays by approximately 65% within 500 ps but then remains roughly constant up to 3 ns. This feature at ~1.9 eV was best fit with a biexponential decay model with a constant offset, $y = A_1 \exp\left(-\frac{t}{\tau_1}\right) + A_2 \exp\left(-\frac{t}{\tau_2}\right) + y_0$. The fit shown in Figure 4c yields time constants of 4 ± 0.5 and 47 ± 5 ps and an offset (y_0) of 0.34. These photoexcited carriers in $LaFeO_3$ likely have lifetimes that extend beyond 3 ns, the length of our experimental delay line. Long lifetimes are critical in efficient light-harvesting devices as they increase the diffusion length of photoexcited carriers allowing the charges to be efficiently collected.

On the basis of a similar analysis for $LaMnO_3$, we find that the transient absorption and reflectance spectra across the visible and near-infrared range, 1.5−4 eV, are derived from heating. Figure S6a compares the thermal difference spectra derived from ellipsometry with the transient absorption spectra, showing that the sign and shape are consistent between the two data sets and confirming the dominant influence of heating. Also, the kinetics in Figures S6b are nearly identical across the visible range, consistent with our interpretation that heat diffusion dominates the kinetic profile. In $LaMnO_3$, we did not see any clear spectral signature in the visible or near-infrared range that we can assign to photoexcited carriers. If there is a below-gap feature as in $LaFeO_3$, it would be below the spectral range of our detector.

Thermal Transport Modeling. After identifying spectral signatures of heat in $LaFeO_3$ and $LaMnO_3$, modeling the time-resolved decay of these features provides a route to quantify thermal conductivity. By fitting the thermal conductivities in monolithic $LaFeO_3$ and $LaMnO_3$, we can then predict the time scales of heat transfer in the bilayers as an independent validation of consistency. Although the underlying principle of TA/TR spectroscopy is similar to time-domain thermoreflectance (TDTR) spectroscopy, TA/TR directly probes the film, whereas TDTR typically utilizes a metal on top of the film of interest to act as an optothermal transducer and monitor the temperature.[47,48] Also in TA/TR spectroscopy, measurements can be performed in a reflection or transmission geometry, can probe films as thin as a few nanometers, and can probe heat transfer through multiple layers within a heterostructure, including selectively probing embedded materials. However, using TA/TR spectroscopy to probe thermal conductivity is most appropriate when heat-induced changes to the real and imaginary part of the refractive index dominate over carrier-induced effects at the probe energies.

Heat transport was modeled with Fick's second law in one dimension:

$$\rho \hat{C}_p \frac{\partial \mathcal{T}}{\partial t} = k \frac{\partial^2 \mathcal{T}}{\partial x^2}$$

where x is distance normal to the surface, $\mathcal{T}$ is temperature, t is time, k is the thermal conductivity, ρ is the density, and $\hat{C}_p$ is the specific heat capacity. The initial temperature profile was modeled assuming that carriers were generated by photoexcitation according to Beer's law and that all excess energy immediately was converted to heat, so that the modeled data starts (t = 0) at a maximum average temperature. Boundary conditions modeled constant heat flux and temperature across the film−substrate interface. At the front surface, the flux was set to zero because preliminary calculations revealed that heat loss via conduction into the substrate or adjacent film was at least 4 orders of magnitude faster than either radiation or convection at the surface. The magnitude of optical response is proportional to temperature up to 250 °C, as determined from

DOI: 10.1021/acs.jpcc.7b09592
J. Phys. Chem. C 2018, 122, 115−123

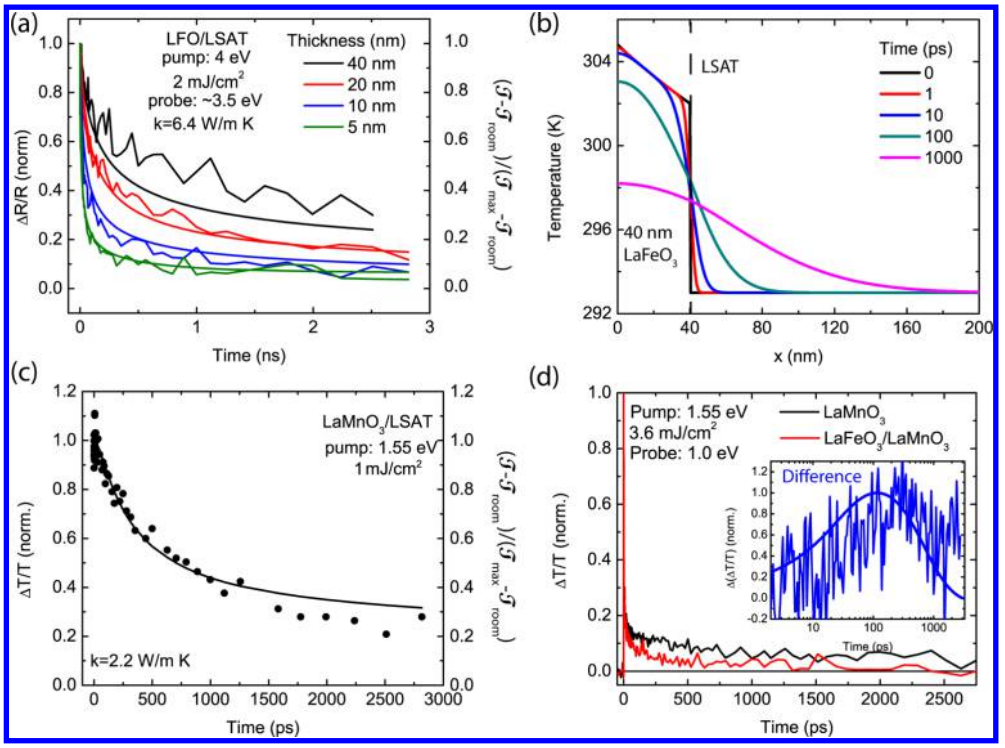

Figure 5. (a) Transient reflectance kinetics for several different thicknesses of $LaFeO_3$ on LSAT, with modeled normalized temperature change within the probe depth (smooth lines). (b) Example model-predicted temperature profiles in $LaFeO_3$ taken at several time delays. (c) Normalized $\Delta T/T$ transient and modeled temperature change in $LaMnO_3$/LSAT with a thermal conductivity of 2.2 W m^{-1} K^{-1}. (d) Normalized $\Delta T/T$ kinetics probed at 1.0 eV in monolithic $LaMnO_3$ and $LaMnO_3$ sandwiched between $LaFeO_3$ and LSAT in the heterostructured film. Inset shows the model-predicted difference in temperature change between the two films (smooth curve) as compared to the experimentally measured difference in kinetics.

ellipsometry and shown in Figure S7. Therefore, the thermal conductivity of the film was fit by minimizing the error between the normalized modeled temperature response within the probe region and the normalized experimental transmission or reflectance change.

To test this model and determine thermal conductivity, four films of different $LaFeO_3$ thickness, ranging from 3 to 25 nm, were grown on single-side polished LSAT. Samples were measured in reflection geometry because the substrate was not double-side polished and because the reflectance signal in the visible range is also dominated by heating above the band gap, making it a probe of film temperature. The films were pumped at 4 eV at the same nominal power, and the kinetics were probed at 3.5 eV, as shown in Figure 5a. The most significant trend is that the thicker films have a slower decay compared to the thinner films; the signal of the 3 nm film decreased by 80% within 100 ps, while the 40 nm film took ~3000 ps to decay by 80%. Given the large temperature gradient at the film–substrate interface, there is a larger driving force for heat transfer in thinner films because the average temperature in those films is higher due to the Beer's law distribution. Also, thinner films have a shorter characteristic length, which makes the characteristic time for heat transfer shorter.

Thermal conductivity was the sole fitting parameter in a global fit of the four $LaFeO_3$ transient reflectance data sets. The heat capacity of $LaFeO_3$ was fixed at 116 J mol^{-1} K^{-1}, within the range reported by Stølen et al.[49] The thermal conductivity of the LSAT substrate was fixed at 5.1 W m^{-1} K^{-1}, according to a manufacturer's reported properties,[50] which is similar to a value of 4.4 W m^{-1} K^{-1} previously reported.[51] An example of the temperature profiles generated by the model is given in Figure 5b. To compare the dynamic response to the TR data, we find the average temperature at each time by integrating over the film thickness. The normalized modeled temperature decay is shown in Figure 5a and matches the experimental reflectance data well with only a single parameter. The best-fit thermal conductivity for thin films of $LaFeO_3$ was 6.4 W m^{-1} K^{-1}, which is slightly higher than the values of 2–3.5 Wm^{-1} K^{-1} reported for other thin film perovskite ferrites, such as $BiFeO_3$.[52,53] Additional heat generation by nonradiative recombination on the time scale of hundreds of picoseconds may cause the slower-than-predicted decay for the thickest film. However, the overall goodness of fit and reasonable fit values suggest that the simple thermal model based on the initial excess photon energy captures the majority of the physics.

To understand the influence of the interface on the modeled kinetics, Kapitza resistance was incorporated in the thermal transport model. Most reported Kaptiza resistance values for epitaxial oxide interfaces vary between 2×10^{-9} and 2×10^{-10} m^2 K W^{-1}.[54−57] Assuming similar values for the $LaFeO_3$/LSAT interface, Figure S8 shows that Kapitza resistance has a minimal effect on the modeled kinetics in $LaFeO_3$.

The TA dynamics of monolithic $LaMnO_3$ film were analogously fit best with a thermal conductivity of 2.2 W m^{-1} K^{-1} (the fit is shown in Figure 5c) and agree reasonably well with literature values which range from 1 to 1.3 W m^{-1} K^{-1}.[58,59]

The approach to modeling heat transfer in monolithic films can also be applied to the bilayer and can predict time scales of heat transfer in heterostructures. In this case, photoexcitation at 1.55 eV generates an initial excess temperature profile in $LaMnO_3$, and the heat subsequently diffuses into both $LaFeO_3$ and the LSAT substrate. As shown in Figure 5d, both monolithic $LaMnO_3$ and a bilayer of $LaFeO_3$/$LaMnO_3$ were excited at the same pump energy of 1.55 eV and fluence of 3.6

DOI: 10.1021/acs.jpcc.7b09592
J. Phys. Chem. C 2018, 122, 115−123

mJ/cm^2 and probed at 1 eV to track the $LaMnO_3$ temperature. After similarly fast decay in both samples for the first ~20 ps, the decay was more rapid over longer time scales in the bilayer because heat conduction into the capping $LaFeO_3$ layer is much faster than radiation or convection to the surrounding air in the monolithic $LaMnO_3$ film. The maximum relative difference between the samples occurs at ~200 ps, as shown in the inset of Figure 5d. The inset also shows a model of the same experimental conditions, which matches the experimental trend and time scale. Deviations between the one-parameter thermal model and experiment may arise due to additional physics that we have neglected here. For instance, recombination of carriers would generate additional heat within the film over time. Nonetheless, this simple model provides essential insight into the transient optical response of the films and enables determination of thermal conductivity.

IV. CONCLUSIONS

We have demonstrated the use of heterojunctions with a type I band alignment to isolate thermal effects from carrier effects in transient optical spectroscopy. Thermal effects dominated the spectra of $LaFeO_3$ and $LaMnO_3$ above their band gaps. Numerical modeling of thermal transport in $LaFeO_3$ and $LaMnO_3$ yielded thermal conductivities of 6.4 and 2.2 $W\ m^{-1}\ K^{-1}$, respectively. A spectral feature below the band gap of $LaFeO_3$ was assigned to photoexcited carriers and persisted for longer than 3 ns, which is promising for light-harvesting applications. This work illustrates that properly accounting for thermal phenomena is critical to the interpretation of transient absorption and reflectance data, specifically to the attribution of carrier-induced changes. Simple thermal modeling can yield predicted time scales of heat transfer and consequently facilitate experimental design to minimize the influence of heating on photoexcited carrier recombination. In addition to its usual intended use for measuring carrier dynamics, TA/TR spectroscopy also provides a contactless means to measure heat transport in monolithic and layered thin films. The approach outlined here can be applied to a wide range of heterostructured materials for optoelectronic and thermal applications.

■ ASSOCIATED CONTENT

Supporting Information

The Supporting Information is available free of charge on the ACS Publications website at DOI: 10.1021/acs.jpcc.7b09592.

Transient reflectance spectra of $LaFeO_3$, $LaMnO_3$, and the $(LaFeO_3)_{52}/(LaMnO_3)_{51}$ bilayer; sample calculation of temperature rise; equations used to convert ellipsometric data to $\Delta T/T$ and $\Delta R/R$; *ex situ* thermal difference spectra for $LaFeO_3$; raw and normalized transient reflectance spectra and kinetics for $LaFeO_3$; discussion of the LSAT substrate contribution; spectral and kinetic transient absorption data for $LaMnO_3$; temperature dependence of $\Delta T/T$ and $\Delta R/R$ for $LaFeO_3$ (PDF)

■ AUTHOR INFORMATION

Corresponding Author

*E-mail jbaxter@drexel.edu (J.B.B.).

ORCID

Jason B. Baxter: 0000-0001-8702-3915

Notes

The authors declare no competing financial interest.

■ ACKNOWLEDGMENTS

The authors acknowledge funding from the National Science Foundation through Grants ECCS-1201957 and DMR-1507988. The ultrafast spectrometer with UV−vis probe at Drexel University was acquired with funds from NSF MRI Award DMR-0922929. Ultrafast experiments in the near-infrared were performed at the Center for Functional Nanomaterials, Brookhaven National Laboratory, which is supported by the U.S. Department of Energy, Office of Basic Energy Sciences, under Contract DE-ACO2-98CH10886. We are grateful to Prof. Caroline Schauer for access to the ellipsometer.

■ REFERENCES

(1) Baxter, J. B.; Richter, C.; Schmuttenmaer, C. A. Ultrafast Carrier Dynamics in Nanostructures for Solar Fuels. *Annu. Rev. Phys. Chem.* **2014**, *65*, 423.

(2) Cargnello, M.; Montini, T.; Smolin, S. Y.; Priebe, J. B.; Delgado Jaén, J. J.; Doan-Nguyen, V. V. T.; McKay, I. S.; Schwalbe, J. A.; Pohl, M.-M.; Gordon, T. R.; et al. Engineering Titania Nanostructure to Tune and Improve its Photocatalytic Activity. *Proc. Natl. Acad. Sci. U. S. A.* **2016**, *113*, 3966−3971.

(3) Stranks, S. D.; Eperon, G. E.; Grancini, G.; Menelaou, C.; Alcocer, M. J. P.; Leijtens, T.; Herz, L. M.; Petrozza, A.; Snaith, H. J. *Science* **2013**, *342*, 341−344.

(4) Yang, Y.; Yan, Y.; Yang, M.; Choi, S.; Zhu, K.; Luther, J. M.; Beard, M. C. Low Surface Recombination Velocity in Solution-Grown $CH_3NH_3PbBr_3$ Perovskite Single Crystal. *Nat. Commun.* **2015**, *6*, 7961.

(5) Prasankumar, R. P.; Upadhya, P. C.; Taylor, A. J. Ultrafast Carrier Dynamics in Semiconductor Nanowires. *Phys. Status Solidi B* **2009**, *246*, 1973−1995.

(6) Sheu, Y. M.; Trugman, S. A.; Park, Y.-S.; Lee, S.; Yi, H. T.; Cheong, S.-W.; Jia, Q. X.; Taylor, A. J.; Prasankumar, R. P. Ultrafast Carrier Dynamics and Radiative Recombination in Multiferroic $BiFeO_3$. *Appl. Phys. Lett.* **2012**, *100*, 242904.

(7) Sabbah, A. J.; Riffe, D. M. Femtosecond Pump-Probe Reflectivity Study of Silicon Carrier Dynamics. *Phys. Rev. B: Condens. Matter Mater. Phys.* **2002**, *66*, 165217.

(8) Yarotski, D. A.; Averitt, R. D.; Negre, N.; Crooker, S. A.; Taylor, A. J.; Donati, G. P.; Stintz, A.; Lester, L. F.; Malloy, K. J. Ultrafast Carrier-Relaxation Dynamics in Self-Assembled InAs/GaAs Quantum Dots. *J. Opt. Soc. Am. B* **2002**, *19*, 1480−1484.

(9) Klimov, V. I. Optical Nonlinearities and Ultrafast Carrier Dynamics in Semiconductor Nanocrystals. *J. Phys. Chem. B* **2000**, *104*, 6112−6123.

(10) Wu, K.; Zhu, H.; Liu, Z.; Rodríguez-Córdoba, W.; Lian, T. Ultrafast Charge Separation and Long-Lived Charge Separated State in Photocatalytic CdS−Pt Nanorod Heterostructures. *J. Am. Chem. Soc.* **2012**, *134*, 10337−10340.

(11) Semonin, O. E.; Luther, J. M.; Choi, S.; Chen, H.-Y.; Gao, J.; Nozik, A. J.; Beard, M. C. *Science* **2011**, *334*, 1530−1533.

(12) Nozik, A. J.; Beard, M. C.; Luther, J. M.; Law, M.; Ellingson, R. J.; Johnson, J. C. Semiconductor Quantum Dots and Quantum Dot Arrays and Applications of Multiple Exciton Generation to Third-Generation Photovoltaic Solar Cells. *Chem. Rev.* **2010**, *110*, 6873−6890.

(13) Zhang, J. Z. Ultrafast Studies of Electron Dynamics in Semiconductor and Metal Colloidal Nanoparticles: Effects of Size and Surface. *Acc. Chem. Res.* **1997**, *30*, 423−429.

(14) Cherepy, N. J.; Liston, D. B.; Lovejoy, J. A.; Deng, H.; Zhang, J. Z. Ultrafast Studies of Photoexcited Electron Dynamics in γ- and α-Fe_2O_3 Semiconductor Nanoparticles. *J. Phys. Chem. B* **1998**, *102*, 770−776.

DOI: 10.1021/acs.jpcc.7b09592
J. Phys. Chem. C 2018, 122, 115−123

(15) Yu, Q.; Meng, X.; Wang, T.; Li, P.; Liu, L.; Chang, K.; Liu, G.; Ye, J. A Highly Durable p-$LaFeO_3$/n-Fe_2O_3 Photocell for Effective Water Splitting Under Visible Light. *Chem. Commun.* **2015**, *51*, 3630−3633.
(16) Hayes, D.; Hadt, R. G.; Emery, J. D.; Cordones, A. A.; Martinson, A. B. F.; Shelby, M. L.; Fransted, K. A.; Dahlberg, P. D.; Hong, J.; Zhang, X.; et al. Electronic and Nuclear Contributions to Time-Resolved Optical and X-ray Absorption Spectra of Hematite and Insights into Photoelectrochemical Performance. *Energy Environ. Sci.* **2016**, *9*, 3754−3769.
(17) Bennett, B. R.; Soref, R. A.; Del Alamo, J. A. Carrier-Induced Change in Refractive Index of InP, GaAs and InGaAsP. *IEEE J. Quantum Electron.* **1990**, *26*, 113−122.
(18) Sjodin, T.; Petek, H.; Dai, H.-L. Ultrafast Carrier Dynamics in Silicon: A Two-Color Transient Reflection Grating Study on a (111) Surface. *Phys. Rev. Lett.* **1998**, *81*, 5664−5667.
(19) Acharya, S.; Chouthe, S.; Graener, H.; Böntgen, T.; Sturm, C.; Schmidt-Grund, R.; Grundmann, M.; Seifert, G. Ultrafast Dynamics of the Dielectric Functions of ZnO and $BaTiO_3$ Thin Films After Intense Femtosecond Laser Excitation. *J. Appl. Phys.* **2014**, *115*, 053508.
(20) Pankove, J. I. *Optical Processes in Semiconductors*; Dover Publications, Inc.: New York, 1971.
(21) Joly, A. G.; Williams, J. R.; Chambers, S. A.; Xiong, G.; Hess, W. P.; Laman, D. M. Carrier Dynamics in α-Fe_2O_3 (0001) Thin Films and Single Crystals Probed by Femtosecond Transient Absorption and Reflectivity. *J. Appl. Phys.* **2006**, *99*, 053521.
(22) Cowan, A. J.; Barnett, C. J.; Pendlebury, S. R.; Barroso, M.; Sivula, K.; Grätzel, M.; Durrant, J. R.; Klug, D. R. Activation Energies for the Rate-Limiting Step in Water Photooxidation by Nanostructured α-Fe_2O_3 and TiO_2. *J. Am. Chem. Soc.* **2011**, *133*, 10134−10140.
(23) Huang, Z.; Lin, Y.; Xiang, X.; Rodriguez-Cordoba, W.; McDonald, K. J.; Hagen, K. S.; Choi, K.-S.; Brunschwig, B. S.; Musaev, D. G.; Hill, C. L.; Wang, D.; Lian, T. In Situ Probe of Photocarrier Dynamics in Water-Splitting Hematite (α-Fe_2O_3) Electrodes. *Energy Environ. Sci.* **2012**, *5*, 8923−8926.
(24) Barroso, M.; Pendlebury, S. R.; Cowan, A. J.; Durrant, J. R. Charge Carrier Trapping, Recombination and Transfer in Hematite (α-Fe_2O_3) Water Splitting Photoanodes. *Chem. Sci.* **2013**, *4*, 2724−2734.
(25) Sorenson, S.; Driscoll, E.; Haghighat, S.; Dawlaty, J. M. Ultrafast Carrier Dynamics in Hematite Films: The Role of Photoexcited Electrons in the Transient Optical Response. *J. Phys. Chem. C* **2014**, *118*, 23621−23626.
(26) Urushibara, A.; Moritomo, Y.; Arima, T.; Asamitsu, A.; Kido, G.; Tokura, Y. Insulator-Metal Transition and Giant Magnetoresistance in $La_{1-x}Sr_xMnO_3$. *Phys. Rev. B: Condens. Matter Mater. Phys.* **1995**, *51*, 14103−14109.
(27) Wadati, H.; Kobayashi, D.; Kumigashira, H.; Okazaki, K.; Mizokawa, T.; Fujimori, A.; Horiba, K.; Oshima, M.; Hamada, N.; Lippmaa, M.; Kawasaki, M.; Koinuma, H. Hole-Doping-Induced Changes in the Electronic Structure of $La_{1-x}Sr_xFeO_3$: Soft X-ray Photoemission and Absorption Study of Epitaxial Thin Films. *Phys. Rev. B: Condens. Matter Mater. Phys.* **2005**, *71*, 035108.
(28) Xie, Y. J.; Scafetta, M. D.; Moon, E. J.; Krick, A. L.; Sichel-Tissot, R. J.; May, S. J. Electronic Phase Diagram of Epitaxial $La_{1-x}Sr_xFeO_3$ Films. *Appl. Phys. Lett.* **2014**, *105*, 062110.
(29) Smolin, S. Y.; Choquette, A. K.; Wilks, R. G.; Gauquelin, N.; Félix, R.; Gerlach, D.; Ueda, S.; Krick, A. L.; Verbeeck, J.; Bär, M.; Baxter, J. B.; May, S. J. Energy Level Alignment and Cation Charge States at the $LaFeO_3$/$LaMnO_3$ (001) Heterointerface. *Adv. Mater. Interfaces* **2017**, *4*, 1700183-n/a.
(30) Goodenough, J. B. Electronic and Ionic Transport Properties and Other Physical Aspects of Perovskites. *Rep. Prog. Phys.* **2004**, *67*, 1915.
(31) Peña, M. A.; Fierro, J. L. G. Chemical Structures and Performance of Perovskite Oxides. *Chem. Rev.* **2001**, *101*, 1981−2018.
(32) Dagotto, E. Complexity in Strongly Correlated Electronic Systems. *Science* **2005**, *309*, 257−262.
(33) Grinberg, I.; West, D. V.; Torres, M.; Gou, G.; Stein, D. M.; Wu, L.; Chen, G.; Gallo, E. M.; Akbashev, A. R.; Davies, P. K.; et al. Perovskite Oxides for Visible-Light-Absorbing Ferroelectric and Photovoltaic Materials. *Nature* **2013**, *503*, 509−512.
(34) Castelli, I. E.; Olsen, T.; Datta, S.; Landis, D. D.; Dahl, S.; Thygesen, K. S.; Jacobsen, K. W. Computational Screening of Perovskite Metal Oxides for Optimal Solar Light Capture. *Energy Environ. Sci.* **2012**, *5*, 5814−5819.
(35) Assmann, E.; Blaha, P.; Laskowski, R.; Held, K.; Okamoto, S.; Sangiovanni, G. Oxide Heterostructures for Efficient Solar Cells. *Phys. Rev. Lett.* **2013**, *110*, 078701.
(36) Wang, L.; Li, Y.; Bera, A.; Ma, C.; Jin, F.; Yuan, K.; Yin, W.; David, A.; Chen, W.; Wu, W.; et al. Device Performance of the Mott Insulator $LaVO_3$ as a Photovoltaic Material. *Phys. Rev. Appl.* **2015**, *3*, 064015.
(37) Yu, L.; Jia, J.; Yi, G. A New-Type Inorganic $[KNbO3]_{0.9}[BaCo_{1/2}Nb_{1/2}O_{3-\delta}]_{0.1}$ Perovskite Oxide as Sensitizer for Photovoltaic Cell. *Phys. Status Solidi A* **2017**, *214*, 1600540-n/a.
(38) Sun, Y.; Wu, X.; Yuan, L.; Wang, M.; Han, M.; Luo, L.; Zheng, B.; Huang, K.; Feng, S. Insight into the Enhanced Photoelectrocatalytic Activity in Reduced $LaFeO_3$ Films. *Chem. Commun.* **2017**, *53*, 2499−2502.
(39) Arima, T.; Tokura, Y.; Torrance, J. B. Variation of Optical Gaps in Perovskite-Type 3d Transition-Metal Oxides. *Phys. Rev. B: Condens. Matter Mater. Phys.* **1993**, *48*, 17006−17009.
(40) Comes, R. B.; Sushko, P. V.; Heald, S. M.; Colby, R. J.; Bowden, M. E.; Chambers, S. A. Band-Gap Reduction and Dopant Interaction in Epitaxial La,Cr Co-doped $SrTiO_3$ Thin Films. *Chem. Mater.* **2014**, *26*, 7073−7082.
(41) Eng, H. W.; Barnes, P. W.; Auer, B. M.; Woodward, P. M. Investigations of the Electronic Structure of d^0 Transition Metal Oxides Belonging to the Perovskite Family. *J. Solid State Chem.* **2003**, *175*, 94−109.
(42) Spanier, J. E.; Fridkin, V. M.; Rappe, A. M.; Akbashev, A. R.; Polemi, A.; Qi, Y.; Gu, Z.; Young, S. M.; Hawley, C. J.; Imbrenda, D.; et al. Power Conversion Efficiency Exceeding the Shockley−Queisser Limit in a Ferroelectric Insulator. *Nat. Photonics* **2016**, *10*, 611−616.
(43) Scafetta, M. D.; Cordi, A. M.; Rondinelli, J. M.; May, S. J. Band Structure and Optical Transitions in $LaFeO_3$: Theory and Experiment. *J. Phys.: Condens. Matter* **2014**, *26*, 505502.
(44) May, K. J.; Fenning, D. P.; Ming, T.; Hong, W. T.; Lee, D.; Stoerzinger, K. A.; Biegalski, M. D.; Kolpak, A. M.; Shao-Horn, Y. Thickness-Dependent Photoelectrochemical Water Splitting on Ultrathin $LaFeO_3$ Films Grown on Nb:$SrTiO_3$. *J. Phys. Chem. Lett.* **2015**, *6*, 977−985.
(45) Parida, K. M.; Reddy, K. H.; Martha, S.; Das, D. P.; Biswal, N. Fabrication of Nanocrystalline $LaFeO_3$: An Efficient Sol−Gel Auto-Combustion Assisted Visible Light Responsive Photocatalyst for Water Decomposition. *Int. J. Hydrogen Energy* **2010**, *35*, 12161−12168.
(46) Smolin, S. Y.; Scafetta, M. D.; Guglietta, G. W.; Baxter, J. B.; May, S. J. Ultrafast Transient Reflectance of Epitaxial Semiconducting Perovskite Thin Films. *Appl. Phys. Lett.* **2014**, *105*, 022103.
(47) Paddock, C. A.; Eesley, G. L. Transient Thermoreflectance from Thin Metal Films. *J. Appl. Phys.* **1986**, *60*, 285−290.
(48) Cahill, D. G.; Ford, W. K.; Goodson, K. E.; Mahan, G. D.; Majumdar, A.; Maris, H. J.; Merlin, R.; Phillpot, S. R. Nanoscale Thermal Transport. *J. Appl. Phys.* **2003**, *93*, 793−818.
(49) Stølen, S.; Grønvold, F.; Brinks, H.; Atake, T.; Mori, H. Heat Capacity and Thermodynamic Properties of $LaFeO_3$ and $LaCoO_3$ from T = 13 K toT = 1000 K. *J. Chem. Thermodyn.* **1998**, *30*, 365−377.
(50) LSAT Single Crystal Substrate; https://www.americanelements.com/lsat-single-crystal-substrate.
(51) Łukasiewicz, T.; Świrkowicz, M.; Sakowska, H.; Turos, A.; Leszczyński, M.; Ratajczak, R. New Oxide Crystal (La,Sr)(Al,Ta)O_3 as Substrate for GaN Epitaxy. *J. Cryst. Growth* **2002**, *237-239*, 1118−1123.
(52) Breckenfeld, E.; Wilson, R.; Karthik, J.; Damodaran, A. R.; Cahill, D. G.; Martin, L. W. Effect of Growth Induced (Non)-

DOI: 10.1021/acs.jpcc.7b09592
J. Phys. Chem. C 2018, 122, 115−123

Stoichiometry on the Structure, Dielectric Response, and Thermal Conductivity of $SrTiO_3$ Thin Films. *Chem. Mater.* **2012**, *24*, 331−337.
(53) Kallaev, S. N.; Omarov, Z. M.; Bakmaev, A. G.; Mitarov, R. G.; Reznichenko, L. A.; Bormanis, K. Thermal Properties of Multiferroic $Bi_{1-x}Eu_xFeO_3$ (x = 0−0.40) Ceramics. *J. Alloys Compd.* **2017**, *695*, 3044−3047.
(54) Wang, Y.; Fujinami, K.; Zhang, R.; Wan, C.; Wang, N.; Ba, Y.; Koumoto, K. Interfacial Thermal Resistance and Thermal Conductivity in Nanograined $SrTiO_3$. *Appl. Phys. Express* **2010**, *3*, 031101.
(55) Costescu, R. M.; Wall, M. A.; Cahill, D. G. Thermal Conductance of Epitaxial Interfaces. *Phys. Rev. B: Condens. Matter Mater. Phys.* **2003**, *67*, 054302.
(56) Liang, X.; Baram, M.; Clarke, D. R. Thermal (Kapitza) Resistance of Interfaces in Compositional Dependent ZnO-In_2O_3 Superlattices. *Appl. Phys. Lett.* **2013**, *102*, 223903.
(57) Buscaglia, M. T.; Maglia, F.; Anselmi-Tamburini, U.; Marré, D.; Pallecchi, I.; Ianculescu, A.; Canu, G.; Viviani, M.; Fabrizio, M.; Buscaglia, V. Effect of Nanostructure on the Thermal Conductivity of La-Doped $SrTiO_3$ Ceramics. *J. Eur. Ceram. Soc.* **2014**, *34*, 307−316.
(58) Cohn, J. L.; Neumeier, J. J.; Popoviciu, C. P.; McClellan, K. J.; Leventouri, T. Local Lattice Distortions and Thermal Transport in Perovskite Manganites. *Phys. Rev. B: Condens. Matter Mater. Phys.* **1997**, *56*, R8495−R8498.
(59) Jha, P.; Sands, T. D.; Jackson, P.; Bomberger, C.; Favaloro, T.; Hodson, S.; Zide, J.; Xu, X.; Shakouri, A. Cross-Plane Thermoelectric Transport in p-Type $La_{0.67}Sr_{0.33}MnO_3/LaMnO_3$ Oxide Metal/Semiconductor Superlattices. *J. Appl. Phys.* **2013**, *113*, 193702.

DOI: 10.1021/acs.jpcc.7b09592
J. Phys. Chem. C 2018, 122, 115−123